Title

Order of Magnitude Sensitivity Increase in X-ray Fluorescence Computed Tomography (XFCT) Imaging With an Optimized Spectro-Spatial Detector Configuration: Theory and Simulation

Journal

IEEE Transactions on Medical Imaging, 33(5)

ISSN

0278-0062

Authors

Ahmad, Moiz
Bazalova, Magdalena
Xiang, Liangzhong
et al.

Publication Date

2014-05-01

DOI

10.1109/tmi.2014.2305101

Peer reviewed

Published in final edited form as:
IEEE Trans Med Imaging. 2014 May ; 33(5): 1119–1128. doi:10.1109/TMI.2014.2305101.

Order of Magnitude Sensitivity Increase in X-ray Fluorescence Computed Tomography (XFCT) Imaging With an Optimized Spectro-Spatial Detector Configuration: Theory and Simulation

Moiz Ahmad, **Magdalena Bazalova**, **Liangzhong Xiang**, and **Lei Xing**
Stanford University School of Medicine, Department of Radiation Oncology, Stanford, CA 94305 USA

Moiz Ahmad: moiz.ahmad@stanford.edu; Magdalena Bazalova: bazalova@stanford.edu; Liangzhong Xiang: xianglzh@stanford.edu; Lei Xing: lei@stanford.edu

Abstract

The purpose of this study was to increase the sensitivity of XFCT imaging by optimizing the data acquisition geometry for reduced scatter X-rays. The placement of detectors and detector energy window were chosen to minimize scatter X-rays. We performed both theoretical calculations and Monte Carlo simulations of this optimized detector configuration on a mouse-sized phantom containing various gold concentrations. The sensitivity limits were determined for three different X-ray spectra: a monoenergetic source, a Gaussian source, and a conventional X-ray tube source. Scatter X-rays were minimized using a backscatter detector orientation (scatter direction > 110° to the primary X-ray beam). The optimized configuration simultaneously reduced the number of detectors and improved the image signal-to-noise ratio. The sensitivity of the optimized configuration was 10 μg/mL (10 pM) at 2 mGy dose with the mono-energetic source, which is an order of magnitude improvement over the unoptimized configuration (102 pM without the optimization). Similar improvements were seen with the Gaussian spectrum source and conventional X-ray tube source. The optimization improvements were predicted in the theoretical model and also demonstrated in simulations. The sensitivity of XFCT imaging can be enhanced by an order of magnitude with the data acquisition optimization, greatly enhancing the potential of this modality for future use in clinical molecular imaging.

Index Terms

Computed tomography (CT) physics; molecular imaging; system design; X-ray imaging

I. Introduction

X-RAY fluorescence computed tomography (XFCT) has been proposed as a modality for element-specific 3-D imaging of a subject [1]–[3]. In this method, X-rays are used to produce fluorescence (characteristic) X-rays through interaction with the high atomic

Correspondence to: Lei Xing, lei@stanford.edu.
Color versions of one or more of the figures in this paper are available online at http://ieeexplore.ieee.org.

number (high-Z) elements present in the imaged object. The detected X-ray fluorescence (XF) signal is used to image the spatial distribution of the high-Z contrast agents. XFCT promises a noninvasive molecular imaging modality of high-Z molecular probes such as gold nano-particles (AuNPs).

Boisseau first demonstrated XFCT imaging in 1986 by imaging the titanium and iron fibers in small (~ 1 mm), sparse (mostly air) samples [1], [2]. Cesareo *et al.* followed soon with XFCT of iodine distributions in small but nonsparse objects [3]. Simionovici *et al.* demonstrated high-resolution X-ray fluorescence micro-tomography in 2000 [4]. In 2008, Takeda *et al.* performed *in vivo* XFCT imaging of iodine perfusion in a mouse brain [5]. All of these experiments used mono-energetic X-rays from synchrotron radiation. Although these studies demonstrated the principle of imaging trace quantities of high-Z contrast materials within a specimen, the cost of a synchrotron facility is prohibitive for clinical and pre-clinical imaging studies. However, to our knowledge, there has been no successful demonstration yet of *in vivo* XFCT using ordinary X-ray sources. One investigation concluded that XFCT using ordinary sources is not competitive with transmission CT when current clinical scan time and imaging dose constraints are applied to both modalities [6]. We focus on XFCT with ordinary poly-energetic X-ray sources, and henceforth refer to XFCT in this context.

Recently, several studies have examined the possibility of XFCT imaging with ordinary poly-energetic X-ray tube sources [7]–[9]. Kuang *et al.* demonstrated imaging of three different elements simultaneously [10]. The main limitation of XFCT for *in vivo* molecular imaging studies is insufficient sensitivity. High sensitivity in molecular probe detection is needed for early detection of disease and therapeutic response assessment. Previous experimental studies using small animal phantoms have demonstrated imaging of gold concentrations as low as 0.5% by weight (5 mg/mL) [7], which is in agreement with previous simulation studies with 0.1% concentration [8], [11]. However, the expected concentration of gold accumulated in tumors using targeted agents is on the order of 0.001% (10 μg/mL) [12], [13]. XFCT has also been proposed as a method for monitoring the uptake of chemotherapy drug Cisplatin, based on the detection of the platinum atom in the drug [8]. Concentrations of 5–40 μg/mL (0.0005%–0.004%) have been measured in cancer patients undergoing Cisplatin chemotherapy [14], [15]. Thus the sensitivity must be greatly improved in order to make XFCT useful for *in vivo* molecular imaging applications.

The imaging sensitivity is limited by the presence of Compton scatter X-ray signal which interferes with the detection of the XF signal. The imaging sensitivity can be dramatically improved by increasing the ratio of XF to Compton photons. In this work, we propose a spatial orientation of detectors such that there is a low probability of acquiring scatter X-rays which have the same energy as fluorescence X-rays (i.e., an optimized spectro-spatial detector configuration).

In this optimization, X-ray detectors are placed at large scattering angles relative to the primary excitation beam. At large scattering angles, the Compton scatter X-rays lose much of their energy in the scattering process. As a result, nearly all of the detected Compton X-rays have a lower energy than the fluorescent X-rays. The two events can then be

distinguished from each other based on detected X-ray energy, and the XF signal to Compton background ratio is greatly increased.

This article is organized as following. In Section II, we develop a theoretical model describing our proposed imaging system. In Section III, we discuss Monte Carlo simulations which allow us to more fully capture the complexity of the physical processes in XFCT. We then provide results from both modeling approaches in Section IV which demonstrate the improvements achieved from the proposed configuration. We close with a discussion and conclusions in Sections V and VI.

II. Theoretical Model

To assess our proposed optimized configuration, we first define a theoretical model to predict the XFCT imaging performance. We then use this model to predict the performance of both the optimized and unoptimized configurations. This model includes the X-ray spectrum, dose, imaged object (phantom), reconstruction parameters and, most importantly, the detector configuration. The figure of merit for performance is the signal-to-noise ratio (SNR). We calculate the raw data SNR as

$$\mathrm{SNR}_{\mathrm{raw}}=\frac{N_{xf}}{\sqrt{N_{xf}+N_{sc}}} \quad (1)$$

where N_{xf} is the number of detected XF photons, and N_{sc} is the number of Compton scatter photons that are indistinguishable from XF photons. We assume that both N_{xf} and N_{sc} have Poisson probability distributions. The scatter signal N_{sc} is included in the noise term $\sqrt{N_{xf}+N_{sc}}$; it becomes large in comparison to N_{xf} at low imaging agent concentrations.

We now calculate N_{xf} and N_{sc} from the X-ray interaction cross sections for X-ray fluorescence and scatter. For photon processes (e.g., absorption, scatter, fluorescence), the number of events N that occur in a thin sample irradiated by I_0 photons is defined as

$$N=I_0 N_t \sigma \quad (2)$$

where σ is the process cross section, and N_t is the number of target atoms or electrons per unit area in the path of the incident photon beam.

Now suppose that a water phantom has a length ℓ in the path of an incident X-ray beam, and that a fraction k_ℓ of this length is a aqueous gold solution region with gold weight percentage k_ρ. Then the number of target gold atoms per unit area available for X-ray fluorescence is

$$N_t=\frac{N_A}{A_{Au}}\cdot(k_\rho \rho_w)\cdot(\ell k_\ell) \quad (3)$$

where N_A is Avogadro's number, A_{Au} is the atomic mass of gold, and ρ_w is the density of water. Combining (2) and (3), we have

$$N_{xf}=I_0 \cdot \left(\frac{N_A}{A_{Au}} k_\rho \rho_w \sigma_{xf}\right) \cdot (\ell k_\ell). \quad (4)$$

For X-ray scattering, the relevant parameter is the number of electrons in the phantom. In our phantom, the X-rays scatter mostly from the water molecules (relatively high abundance of water compared to gold).We calculate the number of target electrons per unit area as

$$Nt=N_A \frac{Z_w}{A_w} \rho_w \cdot \ell \quad (5)$$

where Z_w is the number of electrons per water molecule, and A_w is the atomic mass of water. Combining (2) and (5), we have

$$N_{sc}=I_0 \cdot \left(N_A \frac{Z_w}{A_w} \rho_w \sigma_{sc}\right) \cdot \ell \quad (6)$$

σ_{xf} is an atomic cross section defined in terms of unit area per atom and σ_{sc} is an electronic cross section defined in terms of unit area per electron. See [16] for examples of atomic and electronic cross sections. In the next section, we present the calculation of the cross sections σ_{xf} and σ_{sc} and describe how we include the effects of the detector geometric configuration and X-ray source spectrum into these cross sections.

Combining (1), (4), and (6), we have the following result for the theoretical SNR of the raw data

$$\mathrm{SNR}_{\mathrm{raw}}=\sqrt{I_0 \ell N_A \rho_w}\,\frac{\frac{k_\rho k_\ell \sigma_{xf}}{A_{Au}}}{\sqrt{\frac{k_\rho k_\ell \sigma_{xf}}{A_{Au}}+\frac{\sigma_{sc} Z_w}{A_w}}}. \quad (7)$$

The SNR in the reconstructed image ($\mathrm{SNR}_{\mathrm{recon}}$) also depends on the reconstruction algorithm. If the filtered backprojection reconstruction (FBP) is used, then from the linearity of FBP, the reconstructed image SNR is simply $\mathrm{SNR}_{\mathrm{raw}}$ times a reconstruction factor K_{recon} and the number of projection view angles N_{proj} in the raw data

$$\mathrm{SNR}_{\mathrm{recon}}=K_{\mathrm{recon}} \cdot \sqrt{N_{\mathrm{proj}}} \cdot \mathrm{SNR}_{\mathrm{raw}}. \quad (8)$$

Other reconstruction algorithms such as MLEM [17] can be used instead of FBP for better noise properties, but we used FBP here for its simplicity as a linear transformation. There is usually no analytical closed form K_{recon} for for nonlinear iterative reconstruction algorithms like MLEM. The calculation of the reconstruction factor is K_{recon} presented in Appendix B. Finally, we have the formula for the theoretical SNR in the reconstructed image

$$\mathrm{SNR}_{\mathrm{recon}}=K_{\mathrm{recon}}\sqrt{I_0 N_{\mathrm{proj}}\ell N_A \rho_w}\,\frac{\frac{k_\rho k_\ell \sigma_{xf}}{A_{Au}}}{\sqrt{\frac{k_\rho k_\ell \sigma_{xf}}{A_{Au}}+\frac{\sigma_{sc}Z_w}{A_w}}}. \quad (9)$$

The parameters I_0 and N_{proj} control the radiation dose. Parameters σ_{xf} and σ_{sc} specify the interaction cross sections. Parameters ℓ, k_ℓ, k_ρ characterize the phantom. K_{recon} is the reconstruction factor, and the remaining variables in (9) are physical constants.

This simple theoretical model does not include attenuation of the XF and Compton scatter photons, and assumes a constant X-ray flux throughout the phantom. It also does not account for phantom complexity; it assumes single gold-containing region in the center of a water phantom. Lastly, we did not include higher order effects such as coherent scatter, multiple Compton scatter, or electron binding effects on Compton scatter in our theoretical model, because these are difficult to model theoretically and are negligible. (However, these effects are included in our simulations).

We explicitly considered the energy and spatial distribution of XF and Compton scatter photons in our model. The cross sections σ_{xf} and σ_{sc} are weighted by the spectrum (probability distribution) of the primary X-ray beam; thus, they take the source spectrum into account. They also account for the detector spatial location and the detector energy window, both of which affect the detected number of fluorescence and scatter X-rays. The next section presents the calculation of σ_{xf} and σ_{sc} in our model.

A. Calculation of X-ray Fluorescence and Scatter Cross Sections

The cross section for X-ray fluorescence is the product of the photo-electric cross section and the fluorescent yield

$$\sigma_{xf}(E)=Y_{kk'}\kappa(E) \quad (10)$$

where $\kappa(E)$ is the photoelectric cross section for an incident X-ray with energy E, and the fluorescent yield $Y_{kk'}$ is defined as the probability of a atomic transition from sub-shell k' to sub-shell k given an electron vacancy in shell k. Equation (10) follows from the definition of X-ray fluorescence as a two-step process of photo-electric X-ray absorption (characterized by $\kappa(E)$) followed by a fluorescence photon (characterized by $Y_{kk'}$). We used the empirical tabulated values of $\kappa(E)$ and $Y_{kk'}$ for gold from the Lawrence Livermore National Lab (Livermore, CA, USA) Evaluated Atomic Data Library (EADL) [18].

For a poly-energetic source σ_{xf} must be weighted by the energy probability distribution of the source

$$\sigma_{xf}=Y_{kk'}\int_0^\infty \kappa(E)p(E)\mathrm{d}E. \quad (11)$$

Now suppose we are interested in only the fluorescence emitted in a specific angular range $\theta_1 < \theta < \theta_2$, where θ is the emission angle as defined in Fig. 3. In this case, only the contribution to σ_{xf} from the solid angle defined by θ_1 and θ_2 is calculated

$$\sigma_{xf}(\theta_1,\theta_2)=\frac{Y_{kk'}}{2}\int_{\theta_1}^{\theta_2}\sin\theta \mathrm{d}\theta\int_0^{\infty}\kappa(E)p(E)\mathrm{d}E. \quad (12)$$

(Note that (1/2) $\int_0^{\pi}\sin\theta \mathrm{d}\theta$ integrates to 1 in the case of 4π isotropic geometry). This XF cross section represents the contribution to the total photo-electric cross section from only those photo-electric events that ultimately lead to fluorescent X-rays within scattering angles $\{\theta_1, \theta_2\}$ with a characteristic energy corresponding to a specific electron shell transition.

The calculation of scatter cross section σ_{sc} is derived from the Klein–Nishina theory of X-ray scattering from electrons [19], [20]. We calculate the total scattering cross section as a function of the following parameters: the incident X-ray energy spectrum defined by probability distribution $p(E)$; the scatter energy range $E' \pm \Delta E'/2$; and scattering angle range $\{\theta_1, \theta_2\}$. Given these parameters, the scatter cross section is

$$\sigma_{sc}(E',\Delta E',\theta_1,\theta_2)=2\pi\Delta E'\int_{\theta_1}^{\theta_2}F_{\mathrm{KN}}(E',\theta)p(E'\cdot P(E',\theta))P(E',\theta)^2\sin\theta \mathrm{d}\theta. \quad (13)$$

This energy- and angle-specific cross section represents the contribution of scatter energies $E' \pm \Delta E'/2$ within scattering angles $\{\theta_1, \theta_2\}$ to the total scattering cross section of a poly-energetic X-ray beam. This result is derived in Appendix A. Here, $P(E', \theta)$ is the ratio of the incident photon energy to the scattered photon energy and is given by the Compton scattering formula (see [20])

$$P(E',\theta)=\frac{E}{E'}=1+\left(\frac{E}{m_ec^2}\right)(1-\cos\theta)=\frac{1}{1-\left(\frac{E}{m_ec^2}\right)(1-\cos\theta)} \quad (14)$$

where m_e is the rest energy of an electron (511 keV/c^2). F_{KN} is the Klein–Nishina differential cross section $F_{\mathrm{KN}} = \mathrm{d}\sigma_{sc}/\mathrm{d}\Omega$ for a given scattered photon energy and scattering angle

$$F_{\mathrm{KN}}(E',\theta)=\frac{\mathrm{d}\sigma_{sc}}{\mathrm{d}\Omega}=\alpha^2r_c^2P(E',\theta)^{-2}\frac{\left[P(E',\theta)+\frac{1}{P(E',\theta)}-1+\cos^2\theta\right]}{2} \quad (15)$$

α is the physical fine structure constant (~ 1/137.04) and $r_c = \hbar/m_ec$ is the reduced Compton wavelength of the electron (~ 3.8616×10^{-13} m).We used an energy window $\Delta E' = 1$ keV. The highest energy resolution currently possible in X-ray detectors is about 1 keV for 100-keV X-rays (using high-purity germanium detectors).

The integrals in (12) and (13) cannot be solved analytically because $\kappa(E)$ and $p(E)$ usually do not have closed analytical forms. Therefore, we computed these integrals numerically.

III. Monte Carlo XFCT Simulations

We used the open-source EGSnrc Monte Carlo radiation transport program[21] to simulate XFCT imaging. The Monte Carlo simulation models the transport of photons and electrons, and fully simulates all relevant physical interactions including X-ray fluorescence, bound Compton scattering, coherent scattering, photoelectric interactions, ionization and energy deposition, atomic excitations, and bremsstrahlung. The EGSnrc program takes a set of X-ray beams as an input, and follows the transport of ionizing radiation through a user-specified voxelized phantom. The EGSnrc program accumulates the radiation dose in the phantom, while ignoring radiation that exits the phantom. We modified the EGSnrc program to count all photons that leave the phantom, including primary and secondary X-rays.

A mouse-sized digital phantom of a 2.25 cm diameter was constructed for the simulation study (Fig. 1). The phantom contained four smaller 5-mm-diameter regions of gold nano-particle (AuNP) solutions of various concentrations: 0.001%, 0.002%, 0.005%, and 0.01% by weight. To express this quantity in terms of molar concentration, the nano-particle size (i.e., number of atoms per nano-particle) must be known. We assumed 10-nm-diameter AuNPs, each weighing 5 MDa. We chose this size because the number of atoms per particle was directly measured previously[22], and because it is close to the biologically optimal 30–50 nm range for cellular uptake [23]. The conversion from weight per volume to number of moles per volume is approximately 1 pM per 1 μg/mL of 10-nm-diameter AuNP solution in water. Thus the AuNP concentrations in our simulation were (10, 20, 51, and 102 *pico-molar* respectively). These quantities are listed in Table I. The expected concentration of AuNPs accumulated in tumors using targeted agents is on the order of 0.001% (10 pM for 10-nm AuNPs). [12], [13].

The primary X-ray beam was specified as a rectangular pencil beam of 0.2 mm width in the transverse direction and 1 mm Right: Detector angular position refers to a specific point in the detector array. height in the axial direction. This pencil beam was scanned along the transverse direction in 120 steps for each view angle, and the object was scanned from 360 different views. For each translation and rotational step, each photon leaving the phantom was tallied into one of 400 bins corresponding to an energy range of 0–100 keV. Thus, the data size for each acquisition was 120 × 360 × 400.

A. X-ray Sources

The simulations were performed using three X-rays sources with different energy spectra: a 82 keV monoenergetic spectrum; a Gaussian spectrum with a 82-keV mean and 5-keV standard deviation; and a simulated tungsten anode X-ray tube operated at 110 kVp and filtered with 680 μm of lead. These represent spectra with increasing width. The first two sources are purely theoretical (Delta and Gaussian functions), while the last source was obtained from the simulation of a realistic X-ray producing machine. These X-ray spectra are plotted in Fig. 2.

B. Optimizing the Detector Configuration

We used a spherical array of detectors to detect the XF photons emitted from the imaged object at the center of the sphere (see Fig. 3). The influence of the detector angular position within the array on the number of detected XF and scatter X-rays was first assessed. The emission spectrum was measured at different detector positions. Based on these data, a detector configuration that maximized the ratio of detected XF to scatter X-rays was selected. Specifically, we selected an optimum range of detector position θ within the spherical detector array. (θ is in the (r, θ, φ) spherical coordinate system, with the primary X-ray beam along the longitudinal axis). A value of θ = 0° refers to forward-scattering direction and θ = 180° refers the back-scattering direction.

We assumed that the detector position θ is approximately equal to the scattering angle of scattered X-rays. For our setup with the detectors placed 20 cm away from the center of a 2.5 cm FOV, this is a close approximation. We also assumed a 100% detection efficiency of all X-ray emissions from the phantom. This is only possible with a 4π geometry implemented with a spherical array of detectors encompassing the imaged object. For the optimized detector configuration, we select only part of this spherical array. We chose the spherical detector geometry for maximizing the system sensitivity; however, it is not crucial to this work. As we will show, the important parameter is θ, and the concept of optimizing θ applies just as well to a point detector or a circular ring detector array.

C. Radiation Dose

The influence of dose on imaging outcome is assessed. For each primary X-ray source, we simulated $5 \times 10^8 - 1 \times 10^{11}$ particle histories. These numbers were chosen to correspond to a typical X-ray dose in practice. Although the dose varies slightly among the different X-ray sources, it is roughly 0.1–20 mGy at the surface of the phantom for the range of particle numbers simulated.

D. Data Analysis

We processed the X-ray photon counts from the Monte Carlo simulations into sinogram space data. As described earlier, an spectrum of X-ray counts by energy was acquired for each X-ray pencil beam translation and rotational step for each detector element. We summed these counts among detectors corresponding to a specific range of θ values. We also summed the counts within one of the following 1-keV wide energy windows: 67.0, 68.8, 77.8, and 80.1 keV (corresponding to gold $K_{\alpha 2}$, $K_{\alpha 1}$, $K_{\beta 1}$, and $K_{\beta 2}$ lines, respectively).

Then a basic scatter correction was applied: the phantom was scanned with and without the gold regions. When scanning without the gold regions, the gold concentrations were set to 0, i.e., pure water. The raw data of the pure water phantom were subtracted from the raw sinogram of the gold-containing phantom to produce a scatter-corrected sinogram.

A second scan for scatter correction is not strictly necessary for this work or for XFCT in general; the scatter counts can be interpolated from the acquired spectrum or can be estimated from prior phantom knowledge. Nevertheless, a second scan for scatter measurement provides the best scatter correction and is simple in implementation.

Therefore, we used this scatter correction in our work, and applied it to both the optimized and unoptimized configurations.

The XFCT image was reconstructed from the corrected sinogram data using the filtered back-projection algorithm. A Hamming filter with a cutoff frequency of $0.25 \times f_{Nq}$ was used for smoothing in the reconstruction; f_{Nq} refers to the Nyquist frequency. (f_{Nq} is one-half of the sampling frequency).

The reconstructed images were assessed using the measured SNR metric

$$\mathrm{SNR}=\frac{\mu_A-\mu_B}{\sigma} \quad (16)$$

where μ_A and μ_B are the mean pixel values in two regions of interest (ROI) A and B. σ is the standard deviation of pixel values in region B. ROI *A* was drawn in a region containing gold solution and *B* was drawn in the water background region in the center of the FOV.

IV. Results

A. Optimizing the Detector Configuration

The spectro-spatial distribution of detected X-rays for each of the primary X-ray sources is shown in Fig. 4. The energies of the $K_{\alpha 2}$, $K_{\alpha 1}$, $K_{\beta 1}$, and $K_{\beta 2}$ gold XF lines are 67.0, 68.8, 77.8, and 80.1 keV, respectively, and their intensities are 28%, 48%, 16%, 4%, respectively. Four dashed vertical lines corresponding to the gold X-ray fluorescence energies are annotated for reference. The Compton scatter is anisotropic: back-scatter X-rays ($\theta \approx 180°$) have lower energies than forward-scatter X-rays ($\theta \approx 0°$). On the other hand, the gold X-ray fluorescence is isotropic with a fixed energy and uniform intensity over all angles. The Compton scatter signal overlaps with the XF signal, making the detection of the fluorescence difficult. Nevertheless, there are some detector positions at which the XF signal has little overlap with Compton scatter. Thus, we can select a spatial detector configuration to eliminate or significantly reduce the acquisition of Compton scatter.

We compared four different configurations: $K_{\alpha 1}$ energy window at all values of θ (isotropic); $K_{\alpha 1}$ window at $\theta < 40°$; $K_{\alpha 2}$ window at $\theta < 20°$; and $K_{\beta 1}$ window at $\theta > 110°$. In Fig. 4 it is apparent that the K_{α} lines have the smallest overlap with Compton scatter at small values of detector angular position θ, and K_{β} lines have the smallest overlap with Compton scatter at large values of θ.

These θ ranges were based on the results in Fig. 4, and were then tuned in a trial-and-error approach. We took this approach because strict optimization of θ is a difficult task. This is because the XF-to-scatter ratio and XF intensity are opposing quantities with respect to θ. For instance, consider the $K_{\beta 1}$ window at $\theta > 110°$. As θ increases, the K_{β} lines are increasingly separated in energy from the Compton scatter, reducing the acquisition of Compton scatter. On the other hand, the size of the detector array also decreases, reducing the acquired XF signal. Choosing the optimal θ must balance these two competing requirements. Thus “optimization” must be defined with respect to SNR (or some other quality metric), instead of XF or scatter background intensities. Although we derived an

analytical relationship between SNR and θ in the theoretical model in Part II, the SNR function is neither a smooth nor convex function with respect to θ. The analytical or numerical optimization of SNR on θ is an intractable problem.

Simulation results for these different configurations are shown in Fig. 5. The detection of the $K_{\beta 1}$ X-rays using θ > 110° was the best configuration, despite the fact that the $K_{\beta 1}$ X-rays are only 1/3 as intense as $K_{\alpha 1}$ X-rays and only one half as intense as $K_{\alpha 2}$ X-rays. Furthermore, this configuration used only 1/3 of the detectors compared to the isotropic configuration, because of the restriction θ > 110°. This configuration therefore acquires only 1/9 as many XF photons as the isotropic configuration. On the other hand, the acquisition of scatter X-rays was greatly reduced. In this K_{β} window: θ > 110° configuration, the large scattering angle reduced the energy of the scatter X-rays. Since the energy of the 78 keV gold $K_{\beta 1}$ photons is greater than that of the backscatter X-rays (55–68 keV), the XF and scatter signals were clearly separated by energy discrimination. Contrary to intuition, this configuration simultaneously reduced the number of detectors and improved the imaging result. Using small θ for the K_{α} lines was not better than using the entire isotropic detector array, because the reduction in scatter was not enough to offset the reduction in XF signal in these configurations. Based on these results, this (k_{β} window, θ > 110°) configuration was chosen as the optimal configuration.

B. Optimized Versus Isotropic Configuration

Figs. 6 and 7 display the phantom reconstruction for the simulations with the three X-ray sources and four different imaging doses. The results for the isotropic detector configuration ($K_{\alpha 1}$ window, 0° < θ < 360°) are shown in Fig. 6, while the results for the optimized configuration ($k_{\beta 1}$ window, θ > 110°) are shown in Fig. 7. The intensity of each image was normalized such that the 0.005% concentration region has an intensity of 50 and the 0.01% region has an intensity of 100. The window/level was chosen as [60/30].

In the isotropic detector configuration, the images are degraded by the Compton scatter. For each (X-ray source/dose) setting, the optimized configuration has a better result than the isotropic configuration. The highest concentration recognized at 2.0 mGy dose is 0.01%, even with the monoenergetic source. On the other hand, the lowest 0.001% concentration is recognized with the optimized configuration at the same 2.0 mGy dose. The measured SNRs for the isotropic and optimized simulations were plotted in Fig. 8. Not surprisingly, the best results are obtained with the monoenergetic X-ray source, which is tuned to excite gold atoms with an energy right above the gold K-edge. The measured SNR decreased with broader energy X-ray source spectrum. The 0.001% region was visible at 2.0 mGy dose with the monoenergetic source. With the Gaussian spectrum and filtered 110-kVp X-ray sources, the lowest visible concentration at 2.0 mGy dose was 0.005%. We consider a measured SNR value of 4 as the perceptibility limit based on the Rose criterion [24], and we have marked this value with a dashed line. In a few cases, the measured SNR decreased with increased dose and we attribute this to statistical variation.

C. Comparison of Simulation Results to Theoretical Predictions

We present simulation results and theoretical predictions for the optimized and isotropic configurations. The SNR was measured for both configurations and with various simulation parameters (gold concentration, X-ray dose, and X-ray source spectrum) and compared to the SNR predicted by the theoretical model. The imaging doses ranged from 0.4 mGy to 20 mGy at 0.4 mGy increments. The measured versus predicted SNRs for each of these simulation settings are plotted in Fig. 9 along with a linear regression fit to the data.

Both the theoretical model and the simulations show about a six-fold SNR increase with the optimized configuration compared to the isotropic configuration (left versus right panels). The theoretical model closely matches the simulation results (slope of 0.71 and 0.98; and R^2 = 0.859 and 0.786 for the isotropic and optimized configurations, respectively). A slope of 1.0 means perfect agreement between theory and simulation. Differences between theory and simulations arise because of the simplifying assumptions in the theory. Most importantly, the phantom in the simulations is more complex than the simplified phantom model in theoretical calculations. Despite these differences, there is good agreement between these two independent modeling approaches. Thus our proposed optimization is supported by both theory and simulation.

V. Discussion

The optimized detector configuration simultaneously reduced the number of detectors and improved the image signal-to-noise ratio. This demonstrates the importance of optimizing the detector configuration to acquire data in only the favorable spatial locations. The optimization resulted in an order of magnitude higher sensitivity than with the isotropic configuration. Even though scatter correction was used in both cases, the optimized configuration produced dramatically better results. This is explained by the fact that there is statistical noise in the scatter background which was large compared to the intensity of the XF signal. The scatter statistical noise cannot be removed by scatter correction methods. The optimized configuration reduced the acquisition of scatter in the first place.

There are a few ways to further improve XFCT. First, replacing the analytical filtered back-projection algorithm by a statistical iterative reconstruction algorithm such as maximum likelihood will increase the measured SNR. Secondly, ordinary X-ray sources may be filtered to achieve a narrow energy spectrum.

Currently, the detection limit in experimental XFCT (without synchrotron facilities) has been two orders of magnitude higher than that required in *in vivo* molecular imaging. We were able to make up one order of magnitude with the optimization presented in this work, while the remaining order of magnitude improvement was achieved with simulated instrumentation improvements (large spherical detector array and narrow source X-ray spectra). With these improvements, the sensitivity approaches the requirements for nano-particle based molecular imaging and Cisplatin drug monitoring.

Each molecular imaging modality has important limitations. Clinical molecular imaging is largely performed with nuclear imaging methods (PET and SPECT) because of the exquisite

instrumentation sensitivity (10^{-10} – 10^{-12} M) to positron and gamma emissions. Nevertheless, the nuclear imaging modalities are limited by the short imaging time window imposed by the radioactive decay of imaging probes. This limitation precludes imaging at late times after radio-pharmaceutical administration due to nuclear decay. This poses a limitation in situations with slow imaging agent accumulation and wash-out. Other issues are radiation dose to both patient and health care personnel and expensive radiochemical synthesis of imaging probes. Optical methods, while having excellent sensitivity sensitivity (10^{-9} – 10^{-16} M) in small animal imaging, have limited clinical use because of low penetration of optical photons in large subjects. Conventional MRI has insufficient sensitivity sensitivity (10^{-3} – 10^{-5} M), but hyper-polarization methods are used to increase the SNR in molecular imaging. While promising for imaging fast biochemical kinetics, hyper-polarized MRI is limited to a short imaging time window due to unrecoverable T1 relaxation of hyper-polarized probe. Because of limitations on each of the mentioned modalities, there is a niche for XFCT as a method for molecular imaging in large subjects over a longer imaging time window. The sensitivity in this study was 10 pM (based on 10 μg/mL detectability of nano-particles with approximately 10^6 gold atoms), which is competitive with other nuclear and optical modalities. Our optimized configuration method combined with the proposed instrumentation improvement will enhance the sensitivity of XFCT, making it a viable method in pre-clinical and clinical molecular imaging studies.

VI. Conclusion

An XFCT SNR enhancement technique with an optimized detector configuration was reported in this work. The approach dramatically improves the sensitivity of XFCT by minimizing the acquisition of unwanted scatter X-rays. With this optimized configuration, we demonstrated the feasibility of XFCT for molecular imaging of low concentrations of gold. Our results will guide the design of a future XFCT molecular imaging system.

Acknowledgments

The authors would like to thank G. Pratx and C. Carpenter for their valuable discussions on this work. The authors would also like to thank C. Jenkins for his help with illustrations in this paper.

This work was supported in part by the NCI fellowship under Grant R25T-CA118681, in part by the National Institutes of Health (NIH) under Grant 1R01-EB016777, and in part by the National Institute of Biomedical Imaging and Bioengineering (NIBIB) under Grant 1K99-EB016059.

Appendix A

Derivation of Scattering Cross Section

This appendix derives the energy- and angle-specific scattering cross section σ_{sc} in (13). From the Klein–Nishina theory of X-ray scattering from electrons, the total scatter cross section is calculated by integrating the Klein–Nishina differential cross section F_{KN} over a range of solid angles

$$\sigma_{sc}\int_{\Omega}\left(\frac{\mathrm{d}\sigma_{sc}}{\mathrm{d}\Omega}\right)\mathrm{d}\Omega=\int_{\Omega}F_{\mathrm{KN}}(E',\theta)\mathrm{d}\Omega=2\pi\int F_{\mathrm{KN}}(E',\theta)\sin\theta\mathrm{d}\theta \quad (17)$$

where the F_{KN} is a function of the scattered energy E′ and scattering angle θ. This equation can be found in many radiological physics textbooks (e.g., [20]).

This is the total scattering cross section over all scattered energies and scattering angles from a monoenergetic X-ray source with energy *E*. Each scattering angle has a unique scattered energy which can be found from the Compton scattering formula [(21)].We are interested in only those scattered X-rays that have the same energy as an XF spectral line since these scatter X-rays are indistinguishable from the XF photons. From (17), the fractional contribution by a single scattered energy *E′*to this total cross section is given by the infinitesimal

$$\Delta\sigma_{sc}(E')=2\pi F_{\mathrm{KN}}(E',\theta)\sin\theta\Delta\theta \quad (18)$$

where θ is the scattering angle corresponding to scattered energy *E′*. Δθ is the infinitesimal range of scattering angles corresponding to an infinitesimal energy window Δ*E′*around the scattered energy *E′*.

For a poly-energetic source, scatter X-rays with energy *E′*can be found over a wide range of scattering angles, not just a specific angle. For this source, the contribution from *E′*at a specific θ must be weighted by the probability distribution *p*(*E*) of the poly-energetic source

$$\Delta\sigma_{sc}(E',\theta)=2\pi F_{\mathrm{KN}}(E',\theta)\sin\theta\Delta\theta[p(E)\Delta E]. \quad (19)$$

Δ*E* is the portion of the source spectrum that contributes to scattered energy window Δ*E′*at scattering angle θ. The source energy window Δ*E* depends on θ, whereas Δ*E′*is independent of θ. To modify this expression in terms of Δ*E′*, we make the substitution Δ*E* = (d*E*/d*E′*) Δ*E′*)

$$\Delta\sigma_{sc}(E',\theta)=2\pi F_{\mathrm{KN}}(E',\theta)\sin\theta\Delta\theta\left[p(E)\left(\frac{\mathrm{d}E}{\mathrm{d}E'}\right)\Delta E'\right]. \quad (20)$$

The derivative d*E*/d*E′*is calculated using the Compton energy relation

$$E=E'\cdot P(E',\theta)=\frac{E'}{1-(\frac{E'}{m_ec^2})(1-\cos\theta)}. \quad (21)$$

Using the chain rule for derivatives

$$\frac{\mathrm{d}E}{\mathrm{d}E'}=\frac{1-(\frac{E'}{m_ec^2})(1-\cos\theta)}{(1-(\frac{E'}{m_ec^2})(1-\cos\theta))^2}+\frac{(\frac{E'}{m_ec^2})(1-\cos\theta)}{(1-(\frac{E'}{m_ec^2})(1-\cos\theta))^2}=\left(\frac{1}{1-(\frac{E'}{m_ec^2})(1-\cos\theta)}\right)=P(E',\theta)^2. \quad (22)$$

Combining (20), (21), and (22), we have

$$\Delta\sigma_{sc}(E',\theta)=2\pi F_{\mathrm{KN}}(E',\theta)\sin\theta\Delta\theta\cdot[p(E'\cdot P(E',\theta))P(E',\theta)^2\Delta E']. \quad (23)$$

We integrate (23) over the scattering angles of interest $\{\theta_1, \theta_2\}$ to complete the derivation of (13)

$$\sigma_{sc}(E',\Delta E',\theta_1,\theta_2)=2\pi\Delta E'\int_{\theta_1}^{\theta_2}F_{\mathrm{KN}}(E',\theta)p(E'\cdot P(E',\theta))P(E',\theta)^2\sin\theta\mathrm{d}\theta. \quad (24)$$

Appendix B

Derivation of Reconstruction Factor K_{recon}

This appendix describes the calculation of the multiplicative factor K_{recon} that transforms the raw data SNR into reconstruction SNR. FBP reconstruction involves convolution of the raw data with a filter $R(x)$, where x is the radial direction in the sinogram data. We first calculate the filter $R(x)$. In FBP, $R(x)$ is defined as

$$R(x)=\int_{-f_s/2}^{+f_s/2}w\left(\frac{f}{f_s f_c}\right)|f|\,e^{+i2\pi fx}\mathrm{d}f\quad\frac{-\mathrm{FOV}}{2}<x<\frac{+\mathrm{FOV}}{2} \quad (25)$$

where FOV is the diameter of the scanned field-of-view. $R(x)$ is essentially the (inverse) Fourier transform of the linear ramp function $|f|$. $W(f/f_s f_c)$ is a user-selected windowing function multiplied with the projection data in the frequency domain to add smoothing to the image reconstruction. f_s is the spatial sampling frequency and f_c is the normalized cutoff frequency defined between 0 and 1. f_c selects the maximum frequency in the filtered data. For W, we selected the Hamming window, which is defined as

$$W(f')=\begin{cases}0.54-0.46\cos(2\pi f'), & -1<f'<1\\ 0, & \text{otherwise}\end{cases}. \quad (26)$$

To obtain the reconstruction factor K_{recon}, we first find how the raw data signal mean μ_{raw} and noise σ_{raw} are transformed by convolution with $R(x)$ into mean μ_{recon} and noise σ_{recon} in the reconstruction. μ_{recon} is the weighted average of μ_{raw} over the extent of the gold-containing region x: $\{-k_\ell\cdot\mathrm{FOV}/2, +k_\ell\cdot\mathrm{FOV}/2\}$ by the filter $R(x)$, i.e.,

$$\mu_{\mathrm{recon}}=\int_{-k_\ell\cdot\mathrm{FOV}/2}^{+k_\ell\cdot\mathrm{FOV}/2}\mu_{\mathrm{raw}}R(x)\mathrm{d}x \quad (27)$$

k_ℓ is the fraction of the FOV diameter occupied by the gold-containing region. σ_{recon} is calculated the root mean square weighted average of σ_{raw} over the entire FOV

$$\sigma_{\mathrm{recon}}=\sqrt{\int_{-\mathrm{FOV}/2}^{+\mathrm{FOV}/2}\sigma_{\mathrm{raw}}^2R^2(x)\mathrm{d}x}. \quad (28)$$

We define the reconstruction factor

$$K_{\text{recon}} = \frac{\text{SNR}_{\text{recon}}}{\text{SNR}_{\text{raw}}} = \frac{\frac{\mu_{\text{recon}}}{\mu_{\text{raw}}}}{\frac{\sigma_{\text{recon}}}{\sigma_{\text{raw}}}}. \quad (29)$$

Combining (27), (28), and (29)

$$K_{\text{recon}} = \frac{\int_{-k_\ell \cdot \text{FOV}/2}^{+k_\ell \cdot \text{FOV}/2} R(x)\mathrm{d}x}{\sqrt{\int_{-\text{FOV}/2}^{+\text{FOV}/2} R^2(x)\mathrm{d}x}}. \quad (30)$$

For our choice of Hamming window with a frequency cutoff f_c = 0.25 and k_ℓ = 0.20, we calculated K_{recon} = 0.788. For comparison, K_{recon} = 0.029 for a pure ramp-filter.

References

1. Boisseau, P. Ph.D. dissertation. Cambridge, U.K.: Dept. Phys., Massachusetts Inst. Technol.; 1986. Determination of three dimensional trace element distributions by the use of monochromatic X-ray microbeams.
2. Boisseau P, Grodzins L. Fluorescence tomography using synchrotron radiation at the NSLS. Hyperfine Interact. 1987; 33(1-4):283–292.
3. Cesareo R, Mascarenhas S. A new tomographic device based on the detection of fluorescent X-rays. Nucl. Instrum. Methods Phys. Res. 1989; 277(2):669–672.
4. Simionovici A, Chukalina M, Schroer C, Drakopoulos M, Snigirev A, Snigireva I, Lengeler B, Janssens K, Adams F. High-resolution X-ray fluorescence microtomography of homogeneous samples. IEEE Trans. Nucl. Sci. 2000 Dec; 47(6):2736–2740.
5. Takeda T, et al. X-ray fluorescent CT imaging of cerebral uptake of stable-iodine perfusion agent iodoamphetamine analog IMP in mice. J. Synchrotron Radiat. 2008; 16(1):57–62. [PubMed: 19096175]
6. von Busch H, Harding G, Martens G, Schlomka J-P, Schweizer B. Investigation of externally activated X-ray fluorescence tomography for use in medical diagnostics. Proc. SPIE Med. Imag. 2005:90–101.
7. Cheong S-KL, Jones B, K. Siddiqi A, Liu F, Manohar N, H. Cho S. X-ray fluorescence computed tomography (XFCT) imaging of gold nanoparticle-loaded objects using 110 kVp X-rays. Phys.Med. Biol. 2010; 55(3):647. [PubMed: 20071757]
8. Bazalova M, Kuang Y, Pratx G, Xing L. Investigation of X-ray fluorescence computed tomography (XFCT) and K-edge imaging. IEEE Trans. Med. Imag. 2012 Aug; 31(8):1620–1627.
9. Cong W, Shen H, Cao G, Liu H, Wang G. X-ray fluorescence tomographic system design and image reconstruction. J. X-ray Sci. Technol. 2013; 21(1):1–8.
10. Kuang Y, Pratx G, Bazalova M, Meng B, Qian J, Xing L. First demonstration of multiplexed X-ray fluorescence computed tomography (XFCT) imaging. IEEE Trans. Med. Imag. 2013 Feb; 32(2): 262–267.
11. Jones BL, Cho SH. The feasibility of polychromatic conebeam X-ray fluorescence computed tomography (XFCT) imaging of gold nanoparticle-loaded objects: A Monte Carlo study. Phys. Med. Biol. 2011; 56(12):3719. [PubMed: 21628767]
12. Hainfeld J, O'Connor M, Dilmanian F, Slatkin D, Adams D, Smilowitz H. Micro-CT enables microlocalisation and quantification of HER2-targeted gold nanoparticles within tumour regions. Brit. J. Radiol. 2011; 84(1002):526–533. [PubMed: 21081567]
13. Khlebtsov N, Dykman L. Biodistribution and toxicity of engineered gold nanoparticles: A review of *in vitro* and *in vivo* studies. Chem. Soc. Rev. 2011; 40(3):1647–1671. [PubMed: 21082078]

14. Areberg J, Björkman S, Einarsson L, Frankenberg B, Lundqvist H, Mattsson S, Norrgren K, Scheike O, Wallin R. Gamma camera imaging of platinum in tumours and tissues of patients after administration of 191Pt-Cisplatin. Acta Oncol. 1999; 38(2):221–228. [PubMed: 10227445]
15. Jonson R, Börjesson J, Mattsson S, Unsgaard B, Wallgren A. Uptake and retention of platinum in patients undergoing Cisplatin therapy. Acta Oncol. 1991; 30(3):315–319. [PubMed: 2036240]
16. Johns, H.; Cunningham, J. The Physics of Radiology. 4th ed.. Springfield, IL: Charles C. Thomas; 1983. p. 141ch. 5
17. Shepp LA, Vardi Y. Maximum likelihood reconstruction for emission tomography. IEEE Trans. Med. Imag. 1982 Oct; 1(2):113–122.
18. Perkins, ST.; Cullen, D.; Chen, M.; Rathkopf, J.; Scofield, J.; Hubbell, J. Tables and graphs of atomic subshell and relaxation data derived from the LLNL evaluated atomic data library (EADL). Livermore, CA: Tech. Rep. Lawrence Livermore Nat. Lab.; 1991.
19. Klein O, Nishina Y. The scattering of light by free electrons according to Dirac's new relativistic dynamics. Nature. 1928; 122:398–399.
20. Johns, H.; Cunningham, J. The Physics of Radiology. 4th ed.. Springfield, IL: Charles C. Thomas; 1983. p. 177-182.ch. 6
21. Kawrakow, I.; Rogers, D. The EGSnrc code system: Monte Carlo simulation of electron and ohoton transport, Nat. Res. Council Canada, Ottawa, Canada, Rep. PIRS-701. 2000.
22. Hanay M, Kelber S, Naik A, Chi D, Hentz S, Bullard E, Colinet E, Duraffourg L, Roukes M. Single-protein nanomechanical mass spectrometry in real time. Nat. Nanotechnol. 2012; 7(9):602–608. [PubMed: 22922541]
23. Albanese A, S. Tang P, C. Chan W. The effect of nanoparticle size, shape, and surface chemistry on biological systems. Annu. Rev. Biomed. Eng. 2012; 14:1–16. [PubMed: 22524388]
24. Rose, A. Vision: Human and Electronic. New York: Plenum; 1973.

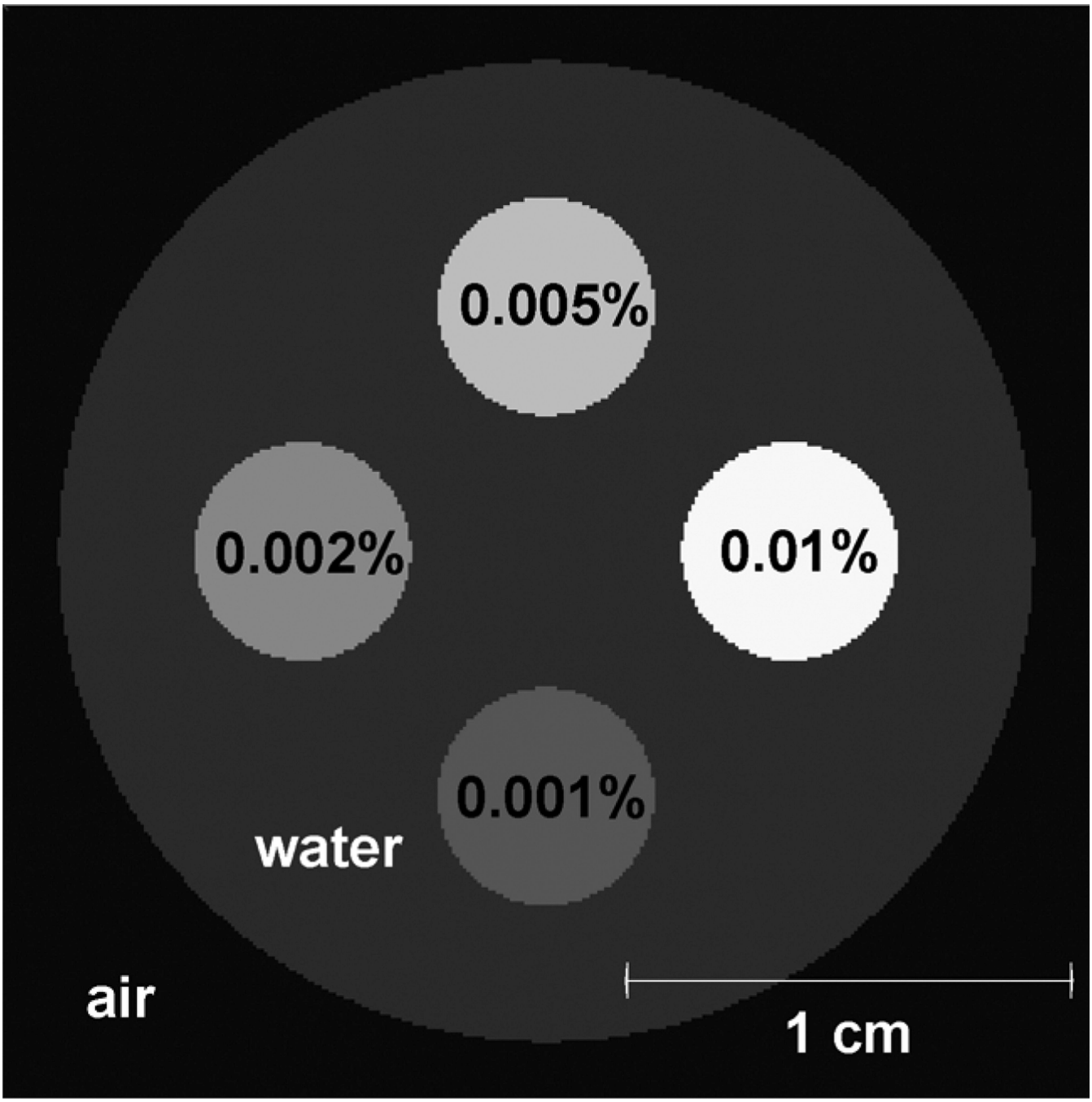

Fig. 1.
Phantom used in XFCT simulations. Regions of various concentrations of gold solution were embedded in a water phantom.

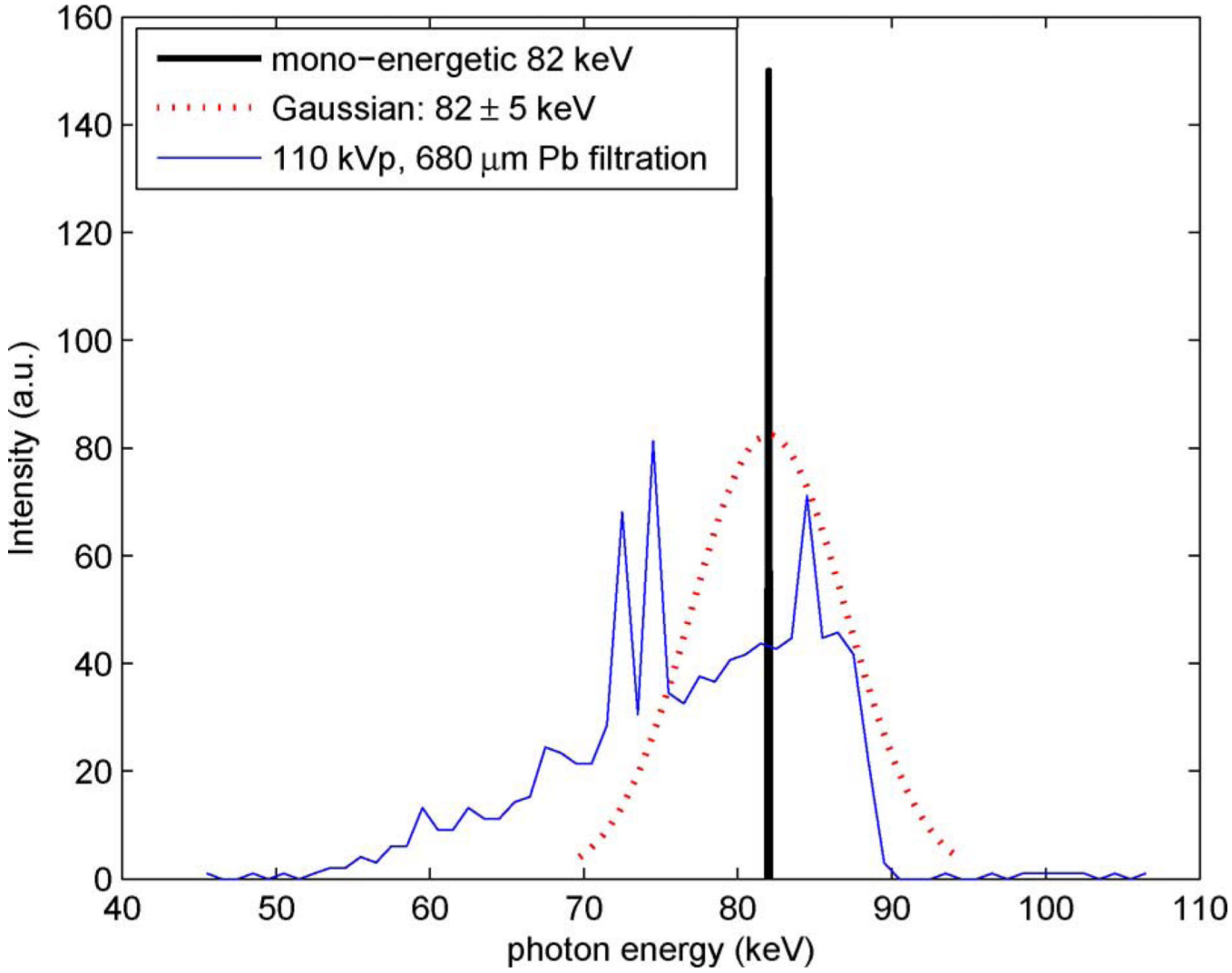

Fig. 2.
X-ray source spectra used in XFCT simulations.

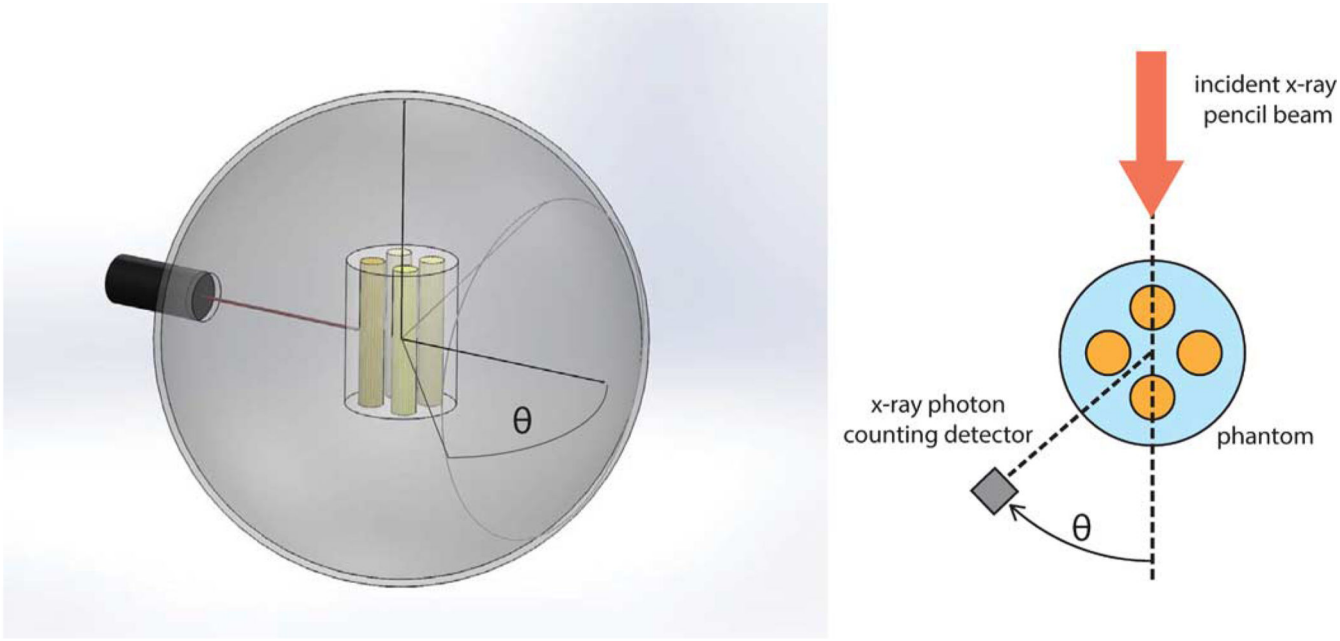

Fig. 3.

XFCT simulation schematics. Left: 3-D illustration of simulated imaging system. Shell of X-ray photon counting detectors surround the scanned object in a 4π geometry. The object is scanned with an X-ray pencil beam. Right: Detector angular position θ refers to a specific point in the detector array.

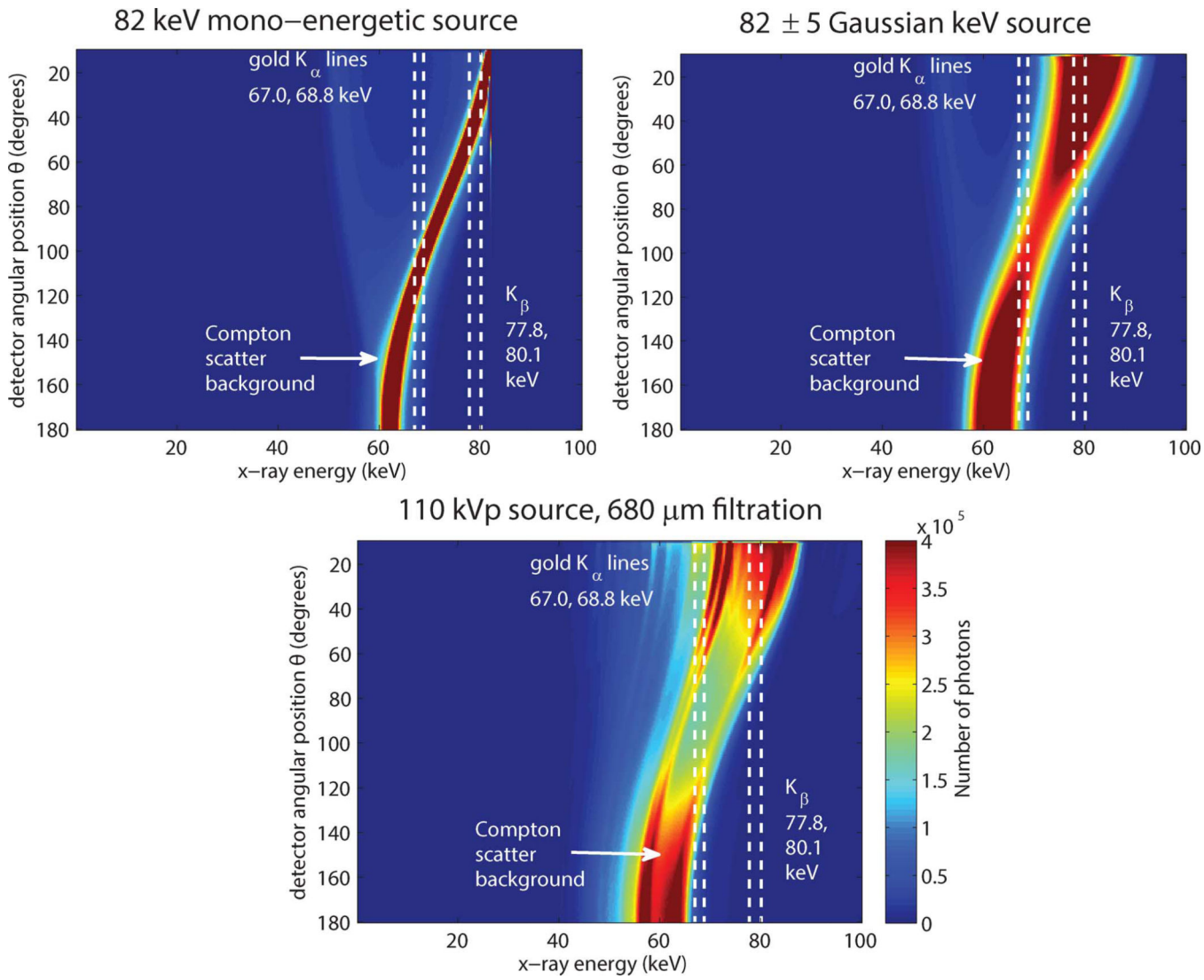

Fig. 4.

The energy and spatial distribution of detected X-rays. Results for three different X-ray sources (monoenergetic 82 keV, Gaussian 82 ± 5 keV, and a 110-kVp X-ray tube source with 680 μm Pb filter) are shown. There were 10^{10} photons in the primary X-ray beam.

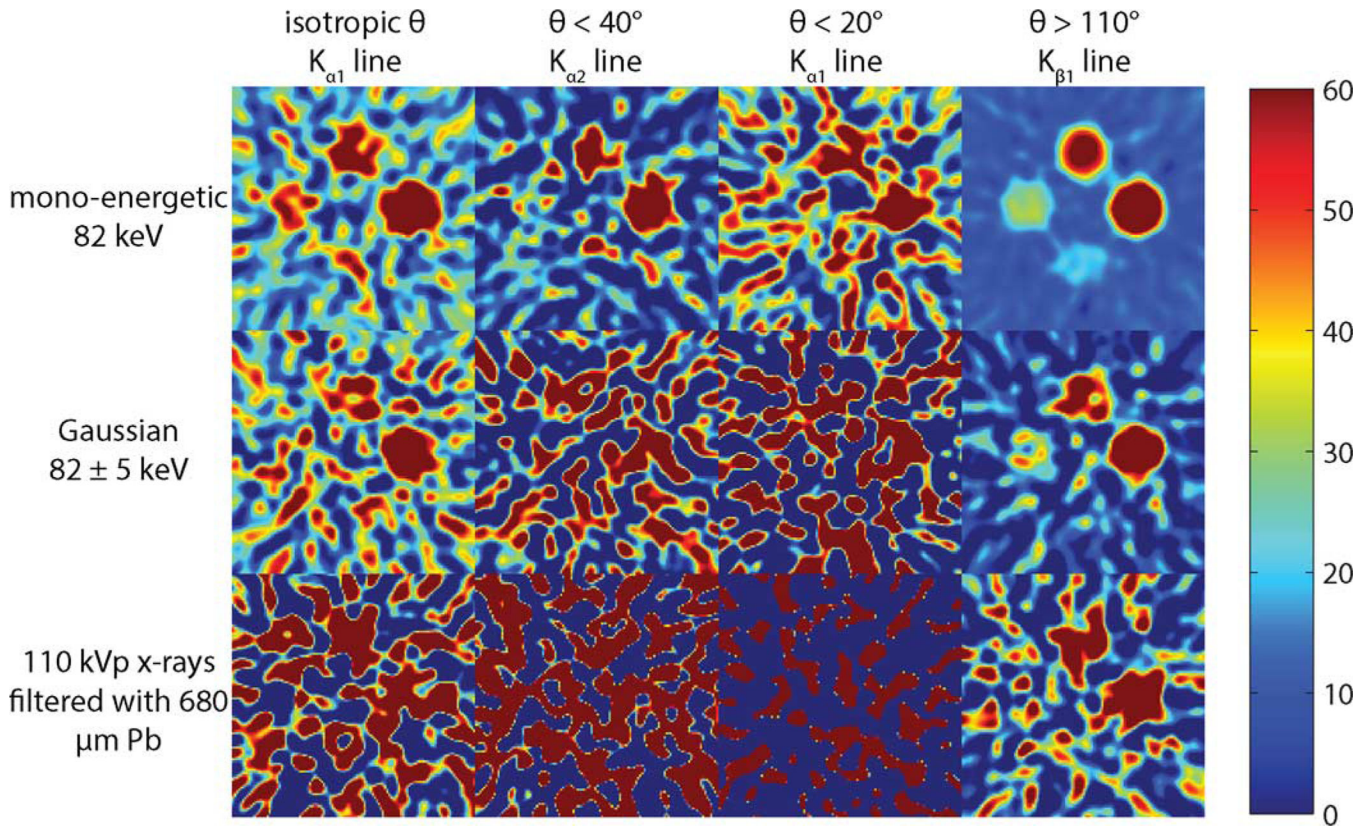

Fig. 5.

Reconstructions corresponding to various detector configurations for 2 mGy dose: 1) $K_{\alpha 2}$ line, Isotropic θ; 2) $K_{\alpha 1}$ line, θ < 40°; 3) $K_{\alpha 2}$ line, θ < 20°; 4) $K_{\beta 1}$ line, θ > 110°. We chose 4) as the optimized detector configuration. Gold concentrations in the phantom were 0.001%, 0.002%, 0.005%, and 0.01%.

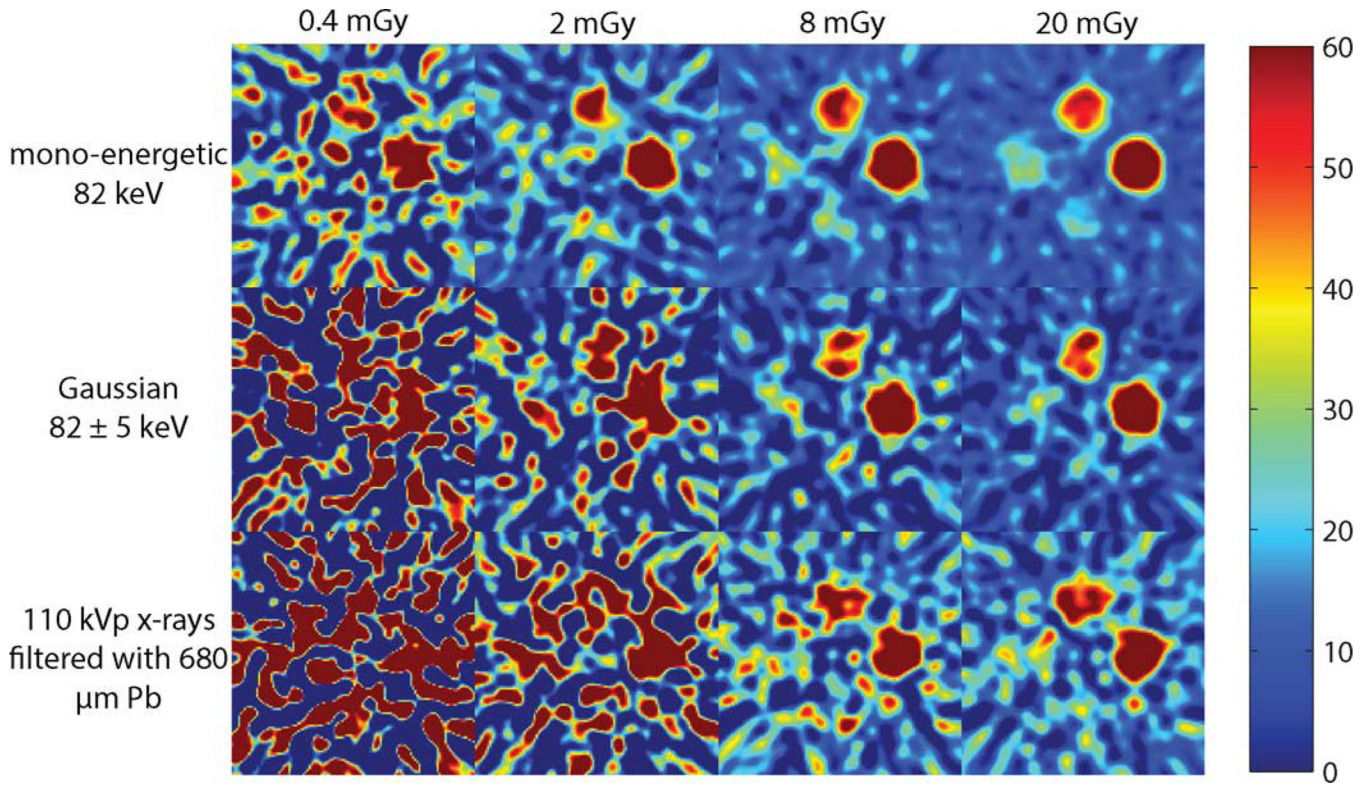

Fig. 6.

XFCT simulation results for the isotropic configuration: 68.8 keV $K_{\alpha 1}$ photons collected at all values of θ. Radiation doses from 0.4 to 20 mGy using three different X-ray spectra. Gold concentrations in the phantom were 0.001%, 0.002%, 0.005%, and 0.01%.

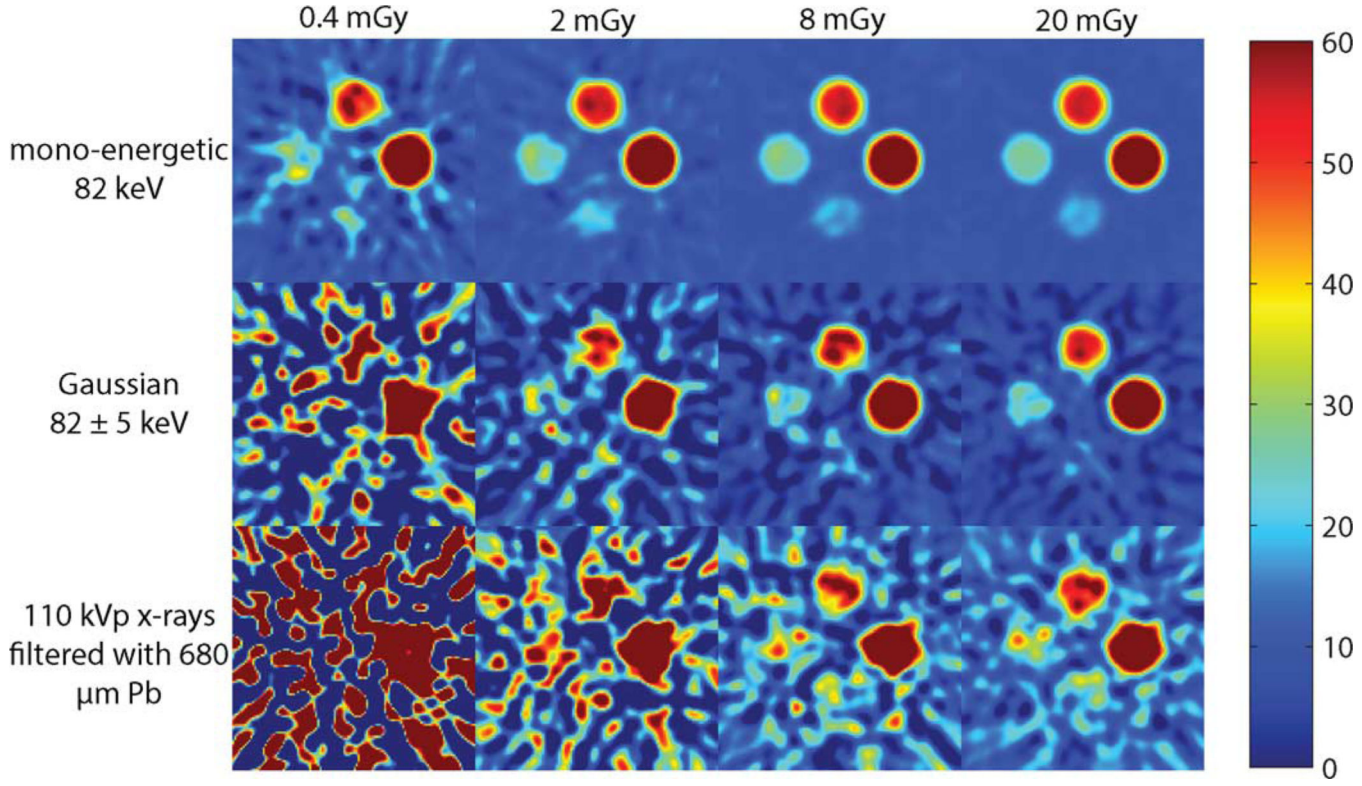

Fig. 7.

XFCT simulation results for the optimized configuration: 78 keV $K_{\beta 1}$ photons collected at $\theta > 110°$. Radiation doses from 0.4 to 20 mGy using three different X-ray spectra. Gold concentrations in the phantom were 0.001%, 0.002%, 0.005%, and 0.01%.

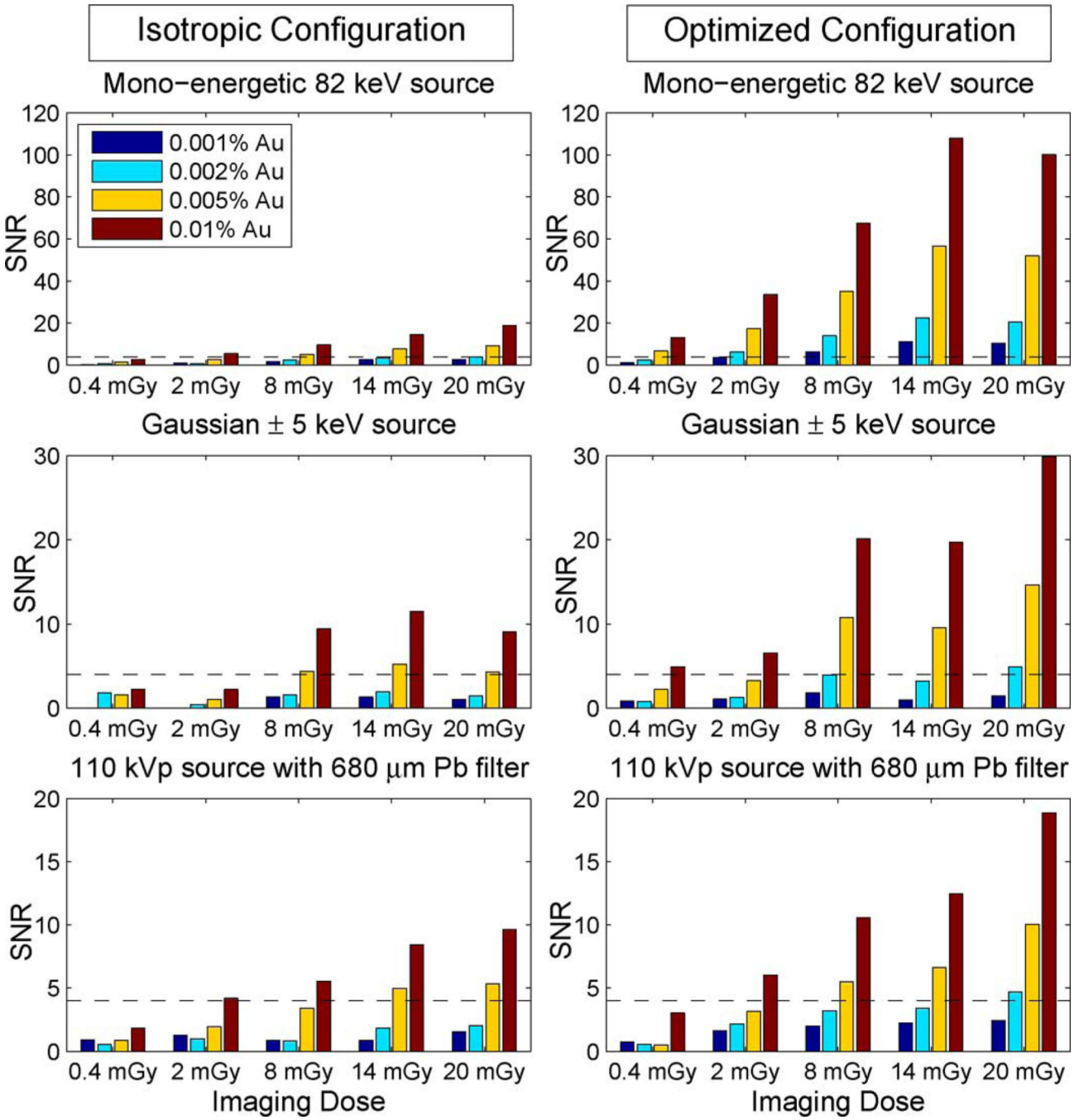

Fig. 8.

SNR values for the isotropic and optimized detector simulations. We used three different sources (monoenergetic 82 keV, Gaussian 82 ± 5 keV, and a 110-kVp X-ray tube source with 680 μm Pb filter). Measured SNRs at various doses and gold concentrations are shown.

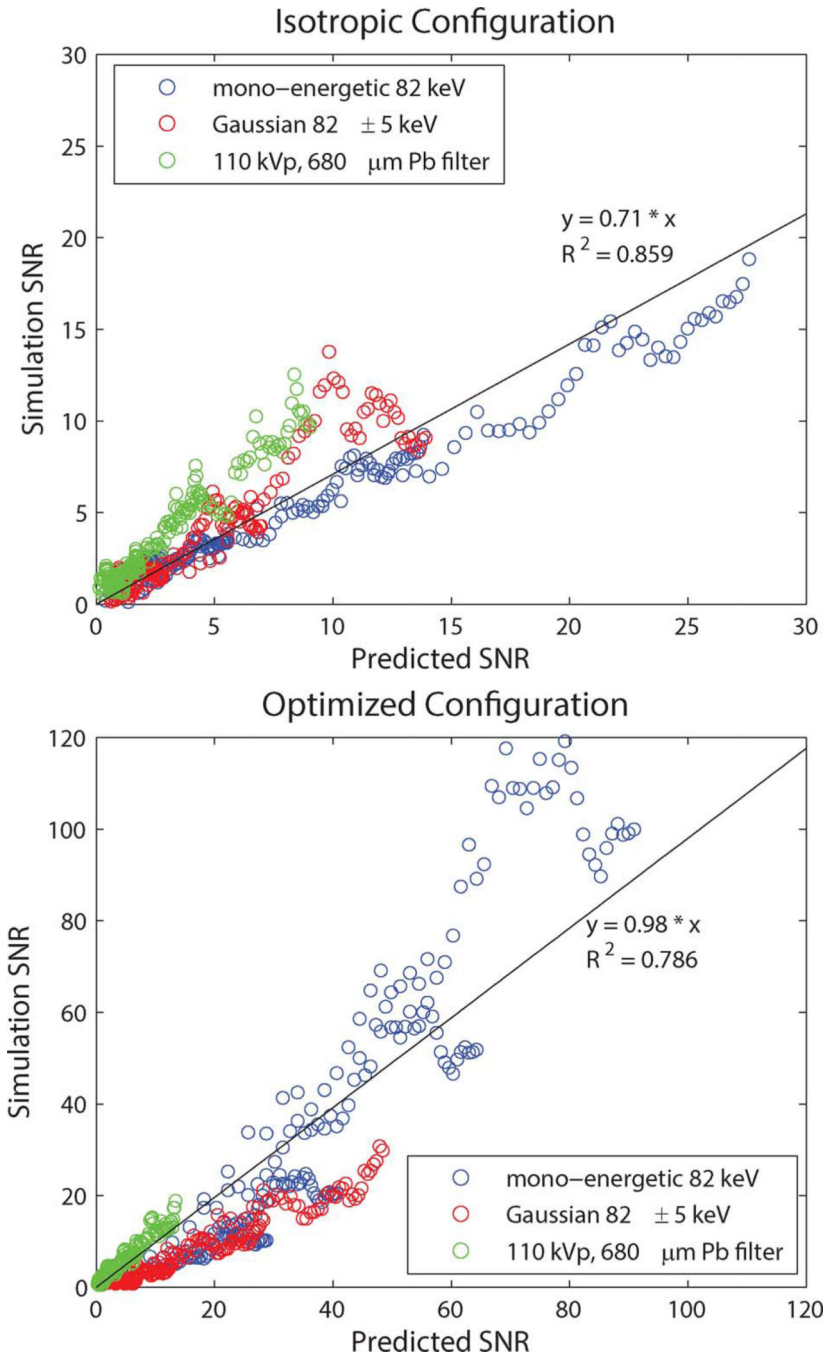

Fig. 9.

Measured versus theoretical SNRs. Left: isotropic configuration; Right: optimized configuration. The data for all gold concentrations, X-ray doses, and X-ray spectra were pooled together.

TABLE I

Gold Concentrations in Phantom in XFCT Simulations. Concentrations Have Been Reported in Different Units

Region	Percent weight	Weight concentration (μg/mL)	Molar concentration (pM)
1	0.001%	10	10
2	0.002%	20	20
3	0.005%	50	51
4	0.010%	100	102